Trade–Off Between Seismic Source Detail and Crustal Heterogeneities in Spherical 3D Finite Element Modeling: the 2004 Sumatra Earthquake case–study

M. Volpe, D. Melini and A. Piersanti
Istituto Nazionale di Geofisica e Vulcanologia
Via di Vigna Murata 605, I-00143 Rome, Italy

Abstract

Finite Element methods (FEMs) are a powerful numerical simulation tool for modeling seismic events as they allow to solve three–dimensional complex models. We used a 3D Finite Element approach to evaluate the co–seismic displacement field produced by the devastating 2004 Sumatra–Andaman earthquake, which caused permanent deformations recorded by continuously operating GPS networks in a region of unprecedented extent. Previous analysis of the static displacement field focused on the heterogeneous distribution of moment release on the fault plane; our intention here is to investigate how much the presence of crustal heterogeneities trades off seismic source details. To this aim, we adopted a quite simple source model in modeling the event. The key feature of our analysis is the generation of a complex three–dimensional spherical domain. Moreover, we also made an accurate analysis concerning boundary conditions, which are crucial for FE simulations.

Key words: finite element method – 3D modeling – static deformation – Sumatra earthquake

1 Introduction

Three-dimensional Finite Element (FE) earthquake simulation is an excellent tool to investigate tectonic deformation, since it allows accurate modeling of geometrically complex domains, complicated faulting systems and heterogeneous material property distributions. In fact, FE modeling can be considered one of the most versatile and accurate numerical methods to solve geophysical problems, even though computationally demanding and intrinsically limited to manage with finite domains. The last point requires to take care of boundary conditions (BC), which still represent an open problem in the FE methods.

This paper is based on a 3D FE earthquake modeling. We present a methodological study aimed at (i) addressing the effect of geometrical and rheological complexities on model–predicted earthquake displacement field on large scale and (ii) demonstrating a trade–off between seismic source details and crustal heterogeneities. We also analyse the impact of numerical artifacts which can be introduced by BC. We used the 2004 Sumatra–Andaman earthquake as a case–study.

The Sumatra event was one of the largest megathrust events of the last century, originated from complex slip on the fault along the subduction zone where the oceanic portion of the Indian Plate slides under the Eurasian Plate. Using different datasets and techniques, the magnitude of the event has been estimated within a range of values between $M_w = 9.0$ and $M_w = 9.3$ (Ammon et. al., 2005; Banerjee et al., 2005; Park et al., 2005; Stein & Okal, 2005; Vallée, 2007), depending on assumptions about the fault geometry and the amount of aseismic slip included in the source model. The slip distribution has been estimated from seismic waves (Ammon et. al., 2005; Lay et al., 2005), static offsets (Banerjee et al., 2005; Vigny et al., 2005; Boschi et al., 2006; Subarya et al., 2006), remote

sensing measurements (Meltzner et al., 2006; Subarya et al., 2006; Tobita et al., 2006) and joint seismic–geodetic data (Chlieh et al., 2007). The overall magnitude of the earthquake has been further constrained by Earth's free oscillations (Park et al., 2005; Stein & Okal, 2005). Some moderate–far–field analyses of GPS data, based on laterally homogeneous numerical modeling, explain particular features of the detected quasi–static deformation field in terms of small scale complexities of the slip distribution on the faulting plane (Banerjee et al., 2005; Boschi et al., 2006).

On the contrary, we adopted a quite simple source model, based on five CMT point sources according to Tsai et al. (2005), to study the effects of 3D features, such as sphericity and lateral rheological heterogeneities, on the deformation field produced by the earthquake. To this aim, we used a recently developed FE simulation tool, FEMSA, which is the acronym for "Finite Element Modeling for Seismic Applications" (Volpe et al., 2007). FEMSA is based on CalculiX, a free three–dimensional FE software distributed under the terms of the GNU General Public License (see `http://www.calculix.de`). In addition, we exploited the capabilities of an external mesher, Cubit, from Sandia National Laboratories (see `http://cubit.sandia.org`), a full–featured software toolkit for geometry preparation and robust generation of 2D and 3D FE meshes. We used Cubit to build up a complex and realistic spherical model, marked by 3D meshing with rheological layering and lateral variations of the rheological properties.

The paper is organized as follows: in section 2 we briefly review the computational method; in section 3 we describe the FE model of the investigated area; in section 4 we discuss our results; concluding remarks are summarized in section 5.

2 Computational details

We recently developed a flexible, versatile and robust numerical simulation tool (FEMSA) to investigate crustal deformation produced by arbitrary seismic dislocations by means of the FE method (Volpe et al., 2007). FEMSA is basically a package composed by interface codes designed to automatically embed faulting sources in plane or spherical domains and to set up and run the simulation. The FE analysis is carried out by the CalculiX solver (see `http://www.calculix.de`), a freely distributed 3D structural analysis software.

Dislocations in FE modeling are commonly treated by contact or split–node technique. In the first case, contact interfaces between deformable bodies with stick and finite frictional slip are introduced (Xing & Makinouchi, 2000, 2002; Cianetti et al., 2005); in the second case, special nodes shared by two elements are defined at which the displacement depends upon which element it is referred to (Melosh & Raefsky, 1981). Differently from these approaches, in our simulations we apply the equivalent body force theorem by incorporating seismic sources as appropriate distributions of double couples of forces (Burridge & Knopoff, 1964; Dahlen, 1972). The reason is that CalculiX does not currently allow any of the two mentioned techniques: in fact, contact capabilities are limited to frictionless contact, which turns out to be not suitable to simulate faulting (except for tensile openings), and nodes at the element interface are not splittable.

Actually, FEMSA generates the seismic source as a 0–, 1– or 2–D distribution of double couples, by defining the force field to be applied to suitably selected nodes, according to the fault geometry and the total seismic moment M_0. The rake angle is taken into account by handling oblique slip as a superposition of a pure strike and a pure dip slip mechanism, each having seismic moment $M = M_0|$ | and $M = M_0|$ |, respectively. An almost arbitrary fault geometry can be handled, consistently with the mesh resolution. Depending on the rheology of the domain, the source generation algorithm differently manages the strike and dip angles in defining the fault orientation. For laterally homogeneous domains, the dip angle is fixed during the source generation stage, while, owing to the symmetry properties of the system, arbitrary strike angles are addressed by means of a reference frame rotation of the displacement field produced by the zero–strike fault. This strategy, when applicable, leads to consistent time savings, especially when a large number of models needs to

be computed, for instance when solving an inverse problem; however, it can not be applied if lateral heterogeneities are involved. In such a case, both the strike and the dip angles are considered in setting the fault geometry.

In practice, nodes in groups of four, corresponding to force application points, are suitably picked from the mesh according to the slip vector and, if needed, moved to match the correct orientation, depending on the fault geometry. The force field is then defined by computing the Cartesian components of the forces for each selected node.

A special remark is dedicated to BC, being the FE method limited to manage finite domains.

In the Literature, BC are commonly established by imposing null displacements at the domain boundaries (Megna et al., 2005; Masterlark & Hughes, 2008) or by keeping nodes on the bottom and lateral surfaces fixed in the direction perpendicular to the surface itself (Cianetti et al., 2005).

In a previous paper (Volpe et al., 2007), we carried out an optimization study on BC, resulting in the occurrence of pronounced artificial effects as we approach the edges, when the cited BC were applied. A better though still not optimal solution is achieved with inhomogeneous boundary conditions, by analytically computing the expected displacements at nodes on the bottom and lateral edges. We use the Okada analytical solutions (Okada, 1985, 1992), which allows to investigate crustal deformation within an isotropic elastic half–space, as a reference model. This approach is formally correct only as long as rheologically homogeneous plane domains are treated, while it represents an approximation if rheological heterogeneities and/or a spherical geometry are introduced, as in the present case. This issue will be more thoroughly discussed in section 4.

It is worth stressing that BC are a crucial point in FE simulations, especially when complex domains are involved. The main shortcoming is that, as a matter of fact, any condition applied to a finite 3D domain introduces a non–physical constraint which may shadow the effect of the heterogeneities. A possible solution would be provided by infinite elements, commonly derived from standard finite elements by modifying the shape functions, which are used to extend the FE method to unbounded domain problems (Bettes, 1992; Dong & Selvadurai, 2009). Nevertheless, such an approach does not represent the best solution for our purposes, as it approximates an infinite media, while the peculiarity of the spherical approach is just the finiteness of the domain. The alternative that definitely would allow to bypass the problem is to simulate a self–gravitating sphere representing the entire Earth. This poses many theoretical and computational challenges and will be the goal of our future work.

The FEMSA package is built up to operate in an automatic way. In Figure 1 a schematic block diagram of the simulation procedure is shown: i) the seismic source is generated; ii) the displacement field is analytically calculated according to the Okada model; iii) inhomogeneous BC are formulated and formalized as explained before; iv) the FE simulation is carried out; v) reference frame transformation is applied to the numerical solution to account for model sphericity; vi) in case of laterally homogeneous domain, reference frame rotation is applied to the numerical solution to account for an arbitrary strike angle. Note that the geometry and mesh definition does not appear in the diagram, since it represents an independent pre–processing step for the simulation.

3 The simulation model

The investigation of the crustal deformation produced by the Sumatra earthquake, due to the unusual size of the event, requires a very long range analysis, where curvature effects can not be neglected.

In a previous work (Volpe et al., 2007), we described a first preliminary approach based on a quite rough 3D model (hereinafter referred to as V07) generated through the native CalculiX pre–processor (cgx), an interactive 3D graphical interface. In the present study, in order to improve that model and better account for detailed features, we built up a more complex and realistic model (hereinafter referred to as C01) by means of the Cubit mesher. The advantages in using Cubit over the native CalculiX mesher consist in a stronger automation in both the geometry and mesh generation process,

the capability of achieving unstructured complex meshes and a better control over the mesh density and quality.

Both the V07 and the C01 models are three–dimensional spherical domains, consisting of a portion of spherical zone about 000 km thick and discretized using 0–nodes brick elements. The mesh density is controlled by accomplishing a finer mesh near the seismic source, where high stress and strain gradients are expected, and a coarse mesh in areas of reasonably constant stress, in order to achieve the best trade–off between accuracy of the solution and computational cost of the analysis. We supposed multi–layered elastic domains to investigate the co–seismic deformation field by means of a static calculation.

In the V07 model (Volpe et al., 2007), the domain spans about 9 0 km on the Earth surface. A FE structured mesh was generated, made by 3 3 elements, resulting in 3 nodes. The element size is about 0 km near the source and about 00 km outside from the source region. The model is shown in Figure 2. The rheological parameters were obtained from the volume averaged values of the Lamé constants according to the Preliminary Reference Earth Model (PREM, Dziewonski & Anderson, 1981).

In the C01 model, the domain spans about . 0 km on the Earth surface. We introduced a realistic rheological contrast between continental and oceanic lithosphere, by (conservatively) extracting the 00 m interface from a global seafloor topography model to retrieve the continental margins. The geometrical model is displayed in Figure 3. The domain was discretized generating an unstructured mesh with 9 elements, resulting in 00 nodes. The element size is biased from 0 to 00 km using the paving meshing algorithm in combination with an appropriate adaptive sizing function. A front view of the mesh is shown in Figure 4. The contrast between continental and oceanic lithosphere was introduced for a thickness of 0 km from the surface, composed by four 0–km–thick layers, with rheological parameters for each layer deduced from the depth profiles of seismic velocities and densities provided by Mooney et al. (1998). At depths greater than 0 km, the domain is split in laterally homogeneous layers with variable thickness, whose elastic constants are calculated from the *ak135* velocity model proposed by Kennet et al. (1995).

The seismic source has been modeled with the multiple CMT solution proposed by Tsai et al. (2005), which consists of five point sources, fitting mantle–wave data registered in the 00 00 s period range by the IRIS Global Seismographic Network. All centroid depths are fixed at km. Such a model results in a total seismic moment of . 0 N m, equivalent to a moment magnitude $M_w = 9.3$. Three large slip patches (%, 33% and % of the total moment) are located in the southern region of the fault, while the moment releases further north represent about 9% and % of the total. The focal mechanisms of the five sources change systematically from south to north: the strike rotates clockwise and the slip vectors rotate from nearly pure thrust to oblique slip with a large right–lateral strike slip component. In our simulations, the analysis with multiple sources is actually treated as a superposition of multiple single sources. We remark that the roughness of the adopted source model is intentional in order to point out the trade–off with the real 3D features of the simulation domain.

4 Results and discussion

The models described in the previous section were solved to obtain the co–seismic deformation field produced by the 2004 Sumatra earthquake and the synthetic displacements were compared with a subset of geodetic measurements recorded by continuously operating GPS networks. During the analysis the rheology was modified, generating a set of FE models as summarized in Table 1. Also, different BC were experimented, using the Okada analytical solution as described before. It is beyond any doubt that such an approximation, neglecting both curvature and lateral heterogeneities, when assigned to an heterogeneous spherical domain introduces a bias on the simulation results and influences the data fit. Nevertheless the goal of the present work is not to give an improvement in modeling the Sumatra

static deformation with respect to published works (e.g. Chlieh et al. (2007)), but to investigate the role of rheological complexities and the trade–off with the source details. In any case, we considered that our approximation improves the implementation of BC with respect to the "standard" choice of assuming zero displacement along the boundaries, which dumps the deformation and would require a larger model size (see Figure 5).

It is dutiful to say that in the very far–field the recorded offsets are not fitted by our calculations; a similar effect has been detected with other approaches (Banerjee et al., 2005; Boschi et al., 2006), where moreover deformations appear overestimated. In fact, modeling is affected by edge effects at a long distance from the source due to the proximity of the mesh boundaries. In addition, the GPS offsets registered in those regions can not be unambiguously associated with the earthquake, as the occurrence of spurious signals can not be excluded.

Instead, we focused our attention on the moderate–far–field (Indian Ocean area) and the Indian region, where other numerical analyses neglecting lateral variations of the rheological properties (Banerjee et al., 2005; Boschi et al., 2006) can fit the measured displacements only by introducing strong constraints on the source model in the form of a highly heterogeneous slip distribution. In these zones we are able to acceptably fit GPS measurements from the dataset obtained by Boschi et al. (2006), holding the well-known limits of our modeling.

As a first step, inhomogeneous averaged BC were applied, by computing the Okada displacements at the boundary nodes using the elastic parameters calculated from the total volume averaged PREM values of the Lamé constants, neglecting rheological layering.

In Figure 6, the synthetic displacements calculated on the V07 and C01 models are compared with GPS data from Boschi et al. (2006). It is worth noting that, in the V07 model, GPS sites are often not coincident with mesh nodes, due to the poor resolution, and the displacement on the closest node is considered in the comparison. On the contrary, the finer mesh of the C01 model allows a more punctual comparison with the GPS datum. In Table 2 the modeled vector magnitude on the inspected sites, their relative error and the misfit with respect to the experimental measurements are compared.

At GPS sites located in the Indian Ocean area the data fit is acceptable, if the roughness of the seismic source model is taken into account. In particular, at the nearest stations (SAMP and NTUS), which are the most sensitive to the detailed source structure, the direction of the modeled vectors is in satisfactory agreement with the observations, while their magnitude is quite underestimated. At the SAMP site the C01 model improves the agreement, while at the NTUS station the V07 model better reproduces the observed offset both in direction and (especially) in magnitude. More important, we remark that a rather good agreement, although the displacements are again underestimated, is found at the Indian sites (HYDE, IISC and BAN2), that Banerjee et al. (2005) and Boschi et al. (2006) managed to fit, with a laterally homogeneous model, only at the cost of introducing a large number of free parameters associated with highly heterogeneous distribution of slip in the source model, which is not confirmed by seismological models. We stress that the poor spatial resolution of the V07 model does not allow to discern between the BAN2 and the IISC stations, due to their small relative distance, while the C01 model does. The vector orientation at the HYDE station is definitely better matched by the C01 model, while the opposite holds for the IISC station. We care to notice that our fit is strongly bound to the geometry of the simulation domain: a test simulation on a multi–layered laterally homogeneous plane domain (hereinafter referred to as P01), with resolution similar to the V07 model, failed in predicting the orientation of the co–seismic displacements at the Indian stations, as is shown in Figure 7. This observation confirms that curvature has an important effect on the computed results.

The comparison between plane and spherical geometry requires a small digression concerning the moderate–far–field. From Figure 7, we note that the static offset at the SAMP station is better reproduced by the P01 than the V07 or C01 models. A similar behaviour is observed in the realm of semi–analytical spherical models, where finite faults are approximated by a superposition of point

sources: in that case, a more precise estimation of moderate–far–field effects is obtained with planar models, where the finite source is fully analytically implemented, since the calculation is not affected by discretization (Piersanti et al., 1997; Nostro et al., 1999). In our simulations, a multiple point source model is introduced in both the plane and the spherical models. Consequently, the difference in the moderate–far–field results has to be accounted as the long–range effect of the Okada BC, which are better matched by the plane model. In this respect, the simulation on the entire sphere is confirmed to be necessary.

Since the dataset of Boschi et al. (2006) is lacking in moderate–far–field data, we also compared our results with GPS measurements from Vigny et al. (2005), focusing on the source region. From Figure 8, we can note that displacements computed with the C01 model are almost systematically shorter than those computed with the V07 model, with few exceptions. In some case this implies a better agreement with GPS offsets (for example at stations KUAL and GETI), while in other cases the fit is worse (for example at stations PHKT and PHUK). Anyway, the orientation of the vectors appears improved in the C01 model with respect to the V07 model.

In order to improve the simulation, we refined BC for the C01 model: we took into account the rheological layering and solved the Okada model for each layer using the appropriate set of elastic constants; the corresponding computed displacements are then prescribed to nodes located on the boundaries of the same layer. In the following, this will be referred to as the C02 model.

From Figure 9, where the comparison with the C01 model and GPS data is shown, and from Table 2, we infer that the upgrading from the C01 to the C02 model has a very little effect on the simulation results.

Ten years ago, Bilek & Lay (1999) estimated rigidity variations with depth along subduction zones interfaces. Rigidity is a measure of the proportionality between shear stress and shear strain and affects the degree of earthquake shaking through its influence on seismic wave speed and earthquake rupture velocity. According to their results, the average rigidity of seismogenic zones appears to increase with depth up to a factor of in the range 0 km. At depths below 0 km, the estimated rigidity values are 3 times lower than in PREM. This result is consistent with the hypothesis that tsunami generating earthquakes, which are typified by large slip and slow rupture velocity, occur in regions of low rigidity at shallow depths. Several mechanisms may contribute to the described trend, but a main role seems to be played by mineralogical phase transitions within the subducting sediments and in the subducting plate, driven by pressure and temperature increasing with depth.

We modified the rheology of the C02 model within a limited region, spanning . 0 km near the source, in order to fit the rigidity trend estimated by Bilek & Lay (1999) in the seismogenic zone. Actually, this means we reduced the rigidity values in the depth range 0 0 km, as indicated in Table 3. In the following, this will be referred to as the C03 model. Figure 11 shows the average rigidity variations in the source region between depths of 0 and 0 km in the C02 and C03 models, compared to the PREM values.

In Figures 12 and 13 we compare the computed vectors and the GPS offsets from the dataset of Boschi et al. (2006) and Vigny et al. (2005), respectively. From Table 2, the Indian sites (HYDE, IISC and BAN2), which are located immediately outside the softened source region, appear as not influenced by the softening; at the nearest stations (SAMP and NTUS), instead, the vector magnitude turns out to be slightly increased, but the effect is very small. Figure 14 displays the ratio between the deformation magnitude calculated with the C03 and C02 models: the rigidity reduction produces a small amplification of the displacements, strictly localized in the source region.

In order to inspect the behaviour of our modeling by emphasizing the softening effect, we reduced the rigidity value by a factor of 3 in the depth range 0 00 km, as indicated in Table 3. In the following, this will be referred to as the C04 model. The comparison with GPS measurements and previous results from the C02 and C03 models, as reported in Figures 12 and 13 as well as in Table 2, shows an amplification of the displacement vectors, but the magnitude of the effect is still very small. The ratio between the deformation magnitude obtained with the C04 and C02 models, shown

in Figure 15, presents a larger amplification with respect to Figure 14, but still strictly localized.

We modified the C04 model applying averaged instead of layered BC, using the average rigidity value of the first 0–km–thick rheological layer. In the following, this will be referred to as the C05 model. The obtained displacements are compared with GPS measurements from Boschi et al. (2006) in Figure 16 and turn out to be greatly increased in magnitude, so that now computed vectors overestimate the GPS offsets. This result is crucial as it demonstrates that BC heavily affect our simulations, in spite of the considerable extent of the simulation domain.

As a last check, we imposed an homogeneous rheology to the C01 model and we adopted the composite source model derived by Tsai et al. (2005). We firstly calculated crustal deformation by using the elastic parameters obtained from the total volume averaged PREM values of the Lamé constants (model C06) and then reducing the rigidity value by a factor of 3 in the whole domain, edges included (model C07). Since within an homogeneous domain under elastic regime a linear stress–strain relationship holds, the ratio between the deformation magnitudes obtained from the two models is expected to be 3 everywhere. This circumstance only occurs if BC are also computed with the reduced rigidity value, as shown in Figure 17. If this is not the case, i.e. if BC are invariably computed using the initial averaged elastic parameters of the C06 model (model C08), a very long range effect of the BC is observed (Figure 18), providing clear evidence that the simulation domain adopted to investigate such a great event, even if large, is not large enough to avoid edge effects also at a short distance from the source, i.e. at a large distance from the boundaries. Future work will be then devoted to build up a totally spherical domain representing the entire Earth, in such a way that the BC issue will be bypassed.

5 Conclusions

By means of a recently developed 3D Finite Element approach (FEMSA), we performed a methodological study concerning the effects of 3D features, such as geometrical and/or rheological heterogeneities, and BC on earthquake modeling. As a case–study, we evaluated the co–seismic displacement field associated with the giant 2004 Sumatra–Andaman earthquake. To this purpose, we generated a complex spherical simulation domain in which a real 3D meshing was introduced as a rheological contrast between continental and oceanic lithosphere. This was achieved by extracting the continental margins from global bathymetry data. We also took into account a realistic variation of the rheological properties with depth in the seismogenic zone, as proposed by Bilek & Lay (1999).

We compared the computed deformation field with GPS measurements using the datasets obtained by Boschi et al. (2006) and Vigny et al. (2005) and paying special attention to the moderate–far–field and the Indian sites. Our results highlight the existence of a trade–off between 3D features and source details and a strong sensitivity to the applied BC.

Presently, most modeling approaches introduce a large number of free parameters to account for small scale complexities of the slip distribution (Boschi et al., 2006; Chlieh et al., 2007), that are not necessarily connected with the physics of the investigated event. We obtained an acceptable agreement with data in the inspected regions using a simple point source model together with a complex spherical 3D meshed simulation domain, where curvature plays a crucial role. The 3D modeling partially trades off the roughness of the source model. Of course we do not mean that there is no need to take into account heterogeneous energy release mechanisms. Our point is that model complexities should be introduced with a logical and physically consistent hierarchy. The presence of major 3D geometrical and rheological features, as sphericity or oceanic crust contrast, is certainly true and, in order to avoid artificial trade–off, their effect should be considered before introducing further complexities as heterogeneous energy release on the fault plane. We remark the occurrence of an asymmetry in the trade–off, since the additional parameters in our simulations are not free parameters but real Earth complexities, which are constrained by the physical properties of the investigated area and can not be arbitrarily tuned.

The systematic analysis of BC revealed a very long range effect on the calculations, even if the simulation domain has a considerably great extent. This result demonstrates that a limited domain, even if large, is not suitable to investigate the effects produced by an event of such a magnitude, requiring the generation of a self–gravitating sphere representing the entire Earth. In this respect, the Sumatra earthquake should be regarded as a real "global" event.

Acknowledgements

The authors are grateful to the CalculiX developers, Guido Dhondt and Klaus Wittig, and to the dedicated exchange forum for the helpful discussions. The Cubit team is also thanked. Special thanks are devoted to Dr. E. Casarotti for the usefull discussions. MV is supported by the MIUR–FIRB research project "Sviluppo di nuove tecnologie per la protezione e la difesa del territorio dai rischi naturali".

References

Ammon, C.J., Ji, C., Thio, H.-K., Robinson, D., Ni, S., Hjorleifsdottir, V., Kanamori, H., Lay, T., Das, S., Helmberger, D., Ichinose, G., Polet, J. & Wald, D., 2005. Rupture Process of the 2004 Sumatra–Andaman Earthquake, *Science*, **308**, 1133–1139.

Banerjee, P., Pollitz, F.F. & Bürgmann, R., 2005. Size and duration of the great 2004 Sumatra–Andaman earthquake from far–field static offsets, *Science*, **308**, 1769–1772.

Bettes, P., 1992. Infinite Elements, *Penshaw Press*, Sunderland, UK, p. 264.

Bilek, S.L. & Lay, T,. 1999. Rigidity variations with depth along interplate megathrust faults in subduction zones, *Nature*, **400**, 443–446.

Bilham, R., Engdahl, R., Feldl, N. & Satyabala, S.P., 2005. Partial and complete rupture of the Indo–Andaman plate boundary 1847–2004, *Seism. Res. Lett.*, **76**, 299–311.

Boschi, E., Casarotti, E., Devoti, R., Melini, D., Piersanti, A., Pietrantonio, G. & Riguzzi, F., 2006. Coseismic deformation induced by the Sumatra earthquake, *J. Geodynamics*, **42**, 52–62.

Burridge, R. & Knopoff, L., 1964. Body force equivalents for seismic dislocations, *Bull. Seism. Soc. Am.* **54**, 1875–1888.

Chlieh, M., Avouac, J.-P., Hjorleifsdottir, V., Song, T.-R.A., Ji, C., Sieh, K., Sladen, A., Hebert, H., Prawirodirdjo, L., Bock, Y. & Galetzka J., 2007. Coseismic Slip and Afterslip of the Great M_w 9.15 Sumatra–Andaman Earthquake of 2004, *Bull. Seism. Soc. Am.* **97**, no. 1A, S152–S173.

Cianetti, S., Giunchi, C. & Cocco, M., 2005. Three–dimensional finite elements modeling of stress interaction: An application to Landers and Hector Mine fault systems, *J. Geophys. Res.* **110**, B05617, doi: 10.1029/2004JB003384.

Dahlen, F.A., 1972. Elastic Dislocation Theory for a Self–Gravitating Elastic Configuration with an Initial Static Stress Field, *Geophys. J. R. Astr. Soc.* **36**, 461–485.

Dewey, J.W., Choy, G., Presgrave, B., Sipkin, S., Tarr, A.C., Benz, H., Earle, P. & Wald, D., 2007. Seismicity associated with the Sumatra–Andaman islands earthquake of December 26, 2004, *Bull. Seism. Soc. Am.* **97**, no. 1A, S25–S42.

Dong, W. & Selvadurai, A.P.S., 2009. A combined finite and infinite element approach for modeling spherically symmetric transient subsurface flow, *Computers & Geosciences* **35**, 438–445.

Dziewonski, A.M & Anderson, D.L., 1981. Preliminary reference Earth model, *Phys. Earth Planet. Inter.* **25**, 297–356.

Kennet, B.L., Engdahl, E.R. & Buland, R., 1995. Constraints on seismic velocities in the Earth from traveltimes, *Geophys. J. Int.* 122, 108–124.

Lay, T., Kanamori, H., Ammon, C.J., Nettles, M., Ward, S.N., Aster, R.C., Beck, S.L., Bilek, S.L., Brudzinski, M.R., Butler, R., DeShon, H.R., Ekström, G., Satake, K. & Sipkin, S., 2005. The Great Sumatra–Andaman Earthquake of 26 December 2004, *Science*, **308**, 1127–1133.

Masterlark, T. & Hughes, K.L.H., 2008. Next generation of deformation models for the 2004 M9 Sumatra–Andaman earthquake, *Geophys. Res. Lett.* **35**, L19310.

Megna, A., Barba, S., & Santini, S., 2005. Normal–fault stress and displacement through finite–element analysis, *Ann. Geophys.*, **48**, 1009–1016.

Melosh, H.J. & Raefsky, A., 1981. A simple and efficient method for introducing faults into finite elements computations, *Bull. Seism. Soc. Am.* **71**, 1391–1400.

Meltzner, A.J., Sieh, K., Abrams, M., Agnew, D.C., Hudnut, K.W., Avouac, J.-P. & Natawidjaja, D.H., 2006. Uplift and subsidence associated with the great Aceh–Andaman earthquake of 2004, *J. Geophys. Res.* **111**, B02407, doi 10.1029/2005JB003891.

Mooney, W.D., Laske, G. & Masters, G., 1998. CRUST 5.1: A global crustal model at ° °, *J. Geophys. Res.* **103**, no. B1, 727–747.

Nostro, C., Piersanti, A., Antonioli, A. & Spada, G., 1999. Spherical versus flat models of coseismic and postseismic deformations, *J. Geophys. Res.* **104**, 13115–13134.

Okada, Y., 1985. Surface deformation due to shear and tensile faults in a half–space, *Bull. Seism. Soc. Am.* **75**, 1135–1154.

Okada, Y., 1992. Internal deformation due to shear and tensile faults in a half-space, *Bull. Seism. Soc. Am.* **82**, 1018–1040.

Park, J., Song, T.-R.A., Tromp, J., Okal, E., Stein, S., Roult, G., Clevede, E., Laske, G., Kanamori, H., Davis, P., Berger, J., Braitenberg, C., Van Camp, M., Lei, X., Sun, H., Xu, H. & Rosat S., 2005. Earth's Free Oscillations Excited by the 26 December 2004 Sumatra–Andaman Earthquake, *Science*, **308**, 1139–1144.

Piersanti, A., Spada, G. & Sabadini, R., 1997. Global postseismic rebound of a viscoelastic Earth: Theory for finite faults and applications to the 1964 Alaska earthquake, *J. Geophys. Res.* **102**, 477–492.

Stein, S. & Okal E., 2005. Speed and Size of the Sumatra Earthquake, *Nature*, **434**, 581–582.

Subarya, C., Chlieh, M., Prawirodirdjo, L., Avouac, J.-P., Bock, Y., Sieh, K., Meltzner, A.J., Natawidjaja, D.H. & McCaffrey R., 2006. Plate–boundary Deformation of the Great Aceh–Andaman Earthquake, *Nature*, **440**, doi 10.1038/nature04522.

Tobita, M., Suito, H., Imakiire, T., Kato, M., Fujiwara, S. & Murakami, M., 2006. Outline of vertical displacement of the 2004 and 2005 Sumatra earthquakes revealed by satellite radar imagery, *Earth Planets Space* **58**, e1–e4.

Tsai, V.C., Nettles, M., Ekstrom, G. & Dziewonsky, A.M, 2005. Multiple CMT source analysis of the 2004 Sumatra earthquake, *Geophys. Res. Lett.* **32**, L17304.

Vallée, M., 2007. Rupture properties of the giant Sumatra earthquake imaged by empirical Green function analysis, *Bull. Seism. Soc. Am.* **97**, no. 1A, S103–S114.

Vigny, C., Simons, W.J.F., Abu, S., Bamphenyu, R., Satirapod, C., Choosakul, N., Subarya, C., Socquet, A., Omar, K., Abidin, H.Z. & Ambrosius B.A.C., 2005. Insight into the 2004 Sumatra–Andaman earthquake from GPS measurements in southeast Asia, *Nature*, **436**, 201–206.

Volpe, M., Melini, D. & Piersanti, A., 2007. FEMSA: A finite element simulation tool for quasi–static deformation modeling, *Ann. Geophys.*, **50**, 367–385.

Xing, H.L. & Makinouchi, A., 2000. A node–to–point contact element strategy and its applications, *RIKEN Rev.: High Performance Computing*, **30**, 35–39.

Xing, H.L. & Makinouchi, A., 2002. Finite element modeling of multi–body contact and its application to active faults, *Concurrency and Computation: Practice and Experience*, **14**, 431–450.

Table 1: Summary of the characteristics of the FE models implemented in the present study.

Model	Geometry	Mesher	Rheology	Lateral heterogeneities	BC	Rigidity softening
V07	spherical	cgx	layered	no	averaged	no
P01	planar	Cubit	homogeneous	no	averaged	no
C01	spherical	Cubit	layered	yes	averaged	no
C02	spherical	Cubit	layered	yes	layered	no
C03	spherical	Cubit	layered	yes	layered	yes
C04	spherical	Cubit	layered	yes	layered	yes
C05	spherical	Cubit	layered	yes	averaged	yes
C06	spherical	Cubit	homogeneous	no	averaged	no
C07	spherical	Cubit	homogeneous	no	averaged	yes
C08	spherical	Cubit	homogeneous	no	averaged	yes

[a] The total volume averaged PREM rigidity value is used.

[b] The layer by layer rigidity values are used.

[c] The first 10–km–thick layer rigidity value is used.

[d] The reduced total volume averaged PREM rigidity value is used.

[e] Applied in the source region in the depth range $10 - 40$ km.

[f] Applied in the source region in the depth range $0 - 100$ km.

[g] Applied in the whole domain.

[h] Applied in the whole domain but the edges.

Table 2: Absolute value of the horizontal displacement vector on a set of GPS sites from the dataset of Boschi et al. (2006) and from FE simulations. The vector magnitude is expressed in cm. The relative error, defined as | | | | | | 00, and the misfit, defined as | | | | , are also indicated between brackets.

	GPS		V07	C01	C02	C03	C04
SAMP	14.62	4%	6.64(-55%,46.8)	6.27(-57%,35.9)	6.33(-57%,34.3)	6.63(-55%,31.9)	8.71(-40%,23.4)
NTUS	2.37	22%	1.50(-37%,4.6)	0.58(-75%,11.3)	0.54(-77%,12.1)	0.55(-77%,12.0)	0.60(-75%,12.3)
HYDE	0.94	38%	0.37(-61%,4.3)	0.50(-47%,4.3)	0.46(-51%,4.1)	0.44(-53%,4.2)	0.46(-51%,4.4)
IISC	1.52	34%	0.82(-46%,4.1)	0.95(-38%,5.3)	0.85(-44%,5.2)	0.85(-44%,5.1)	0.89(-41%,5.4)
BAN2	1.10	43%	/	0.90(-17%,3.4)	0.81(-26%,3.5)	0.81(-26%,3.4)	0.85(-22%,3.6)

Table 3: Rigidity layering used to perform the FE simulations. The softening is only applied in the seismogenic zone. Up to 40 km from the surface the continental and the oceanic lithosphere are differentiated. Numerical values are expressed in units of 0^{0} Pa.

	C01,C02		C03		C04,C05	
	cont.	oce.	cont.	oce.	cont.	oce.
0–10 km	0.58	0.58	0.58	0.58	0.19	0.19
10–20 km	3.43	6.48	0.86	1.62	1.14	2.16
20–30 km	4.33	6.88	1.44	2.29	1.44	2.29
30–40 km	6.48	6.88	2.16	2.29	2.16	2.29
40–180 km	6.71		6.71		2.24	
80–100 km	6.78		6.78		2.26	
100–120 km	6.78		6.78		6.78	
120–140 km	6.87		6.87		6.87	
140–240 km	7.07		7.07		7.07	
240–340 km	7.67		7.67		7.67	
340–670 km	10.9		10.9		10.9	
670–1000 km	17.3		17.3		17.3	

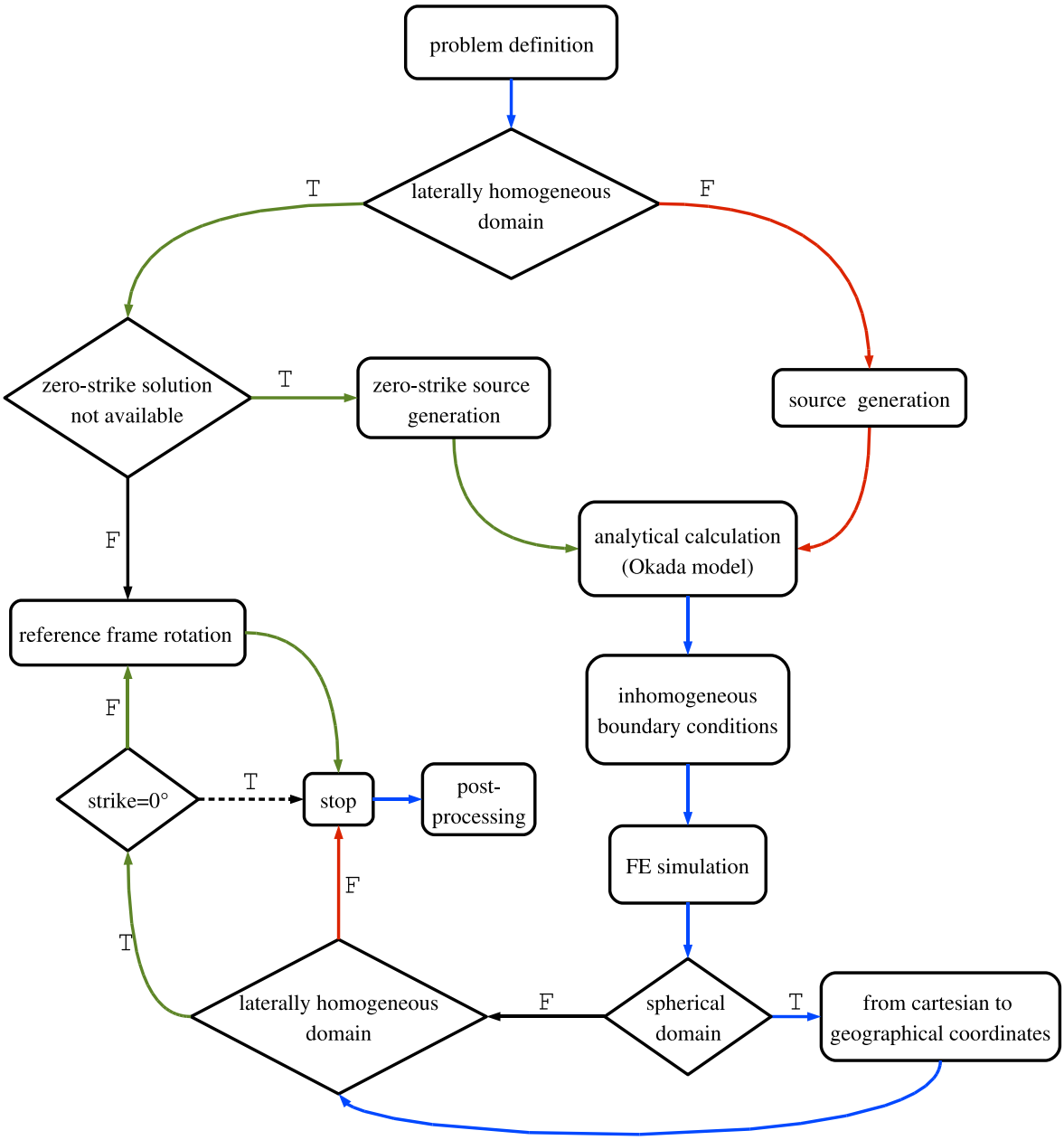

Figure 1: Block diagram of the automatic simulation procedure implemented in FEMSA, as described in the text. The green path is related to laterally homogeneous domains, the red path is related to domains with lateral variations of the rheological properties, while the blue path is shared between the two types of domain.

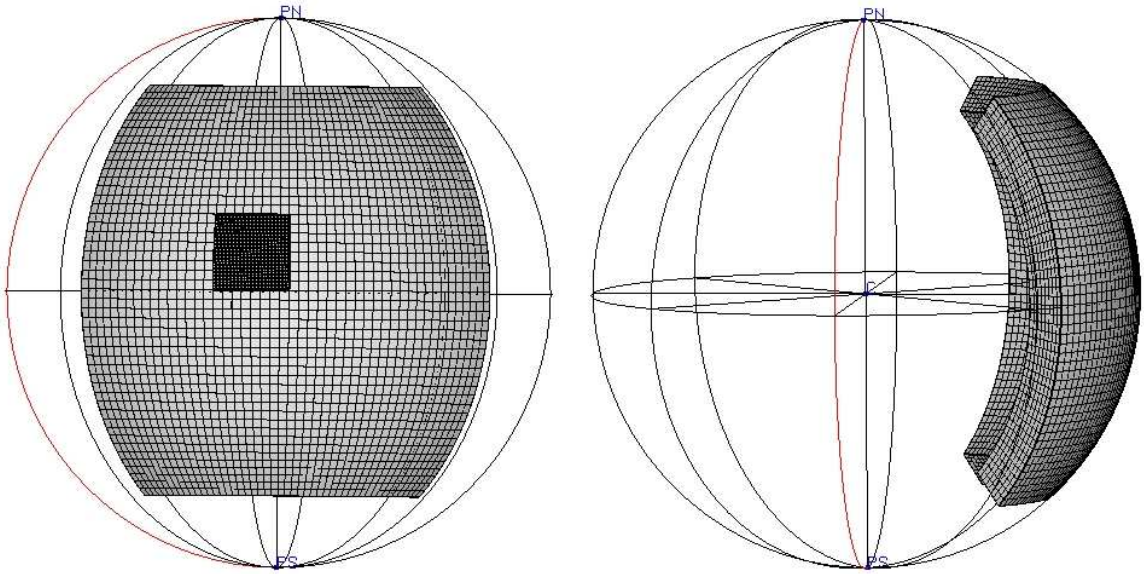

Figure 2: Front and lateral view of the mesh generated by cgx (Volpe et al., 2007). The wireframed sphere is only displayed for presentation purposes.

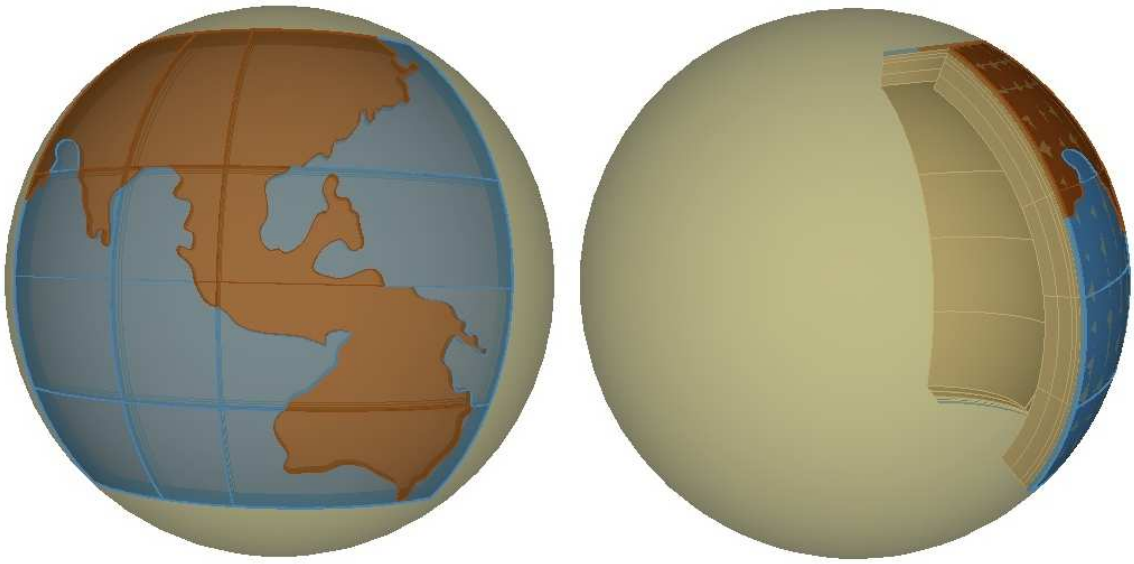

Figure 3: Pictorial view of the model generated by Cubit. A front and a lateral perspective of the domain are shown, both being represented on the sphere for a better view. The contrast between the continental and the oceanic lithosphere is emphasized by colours.

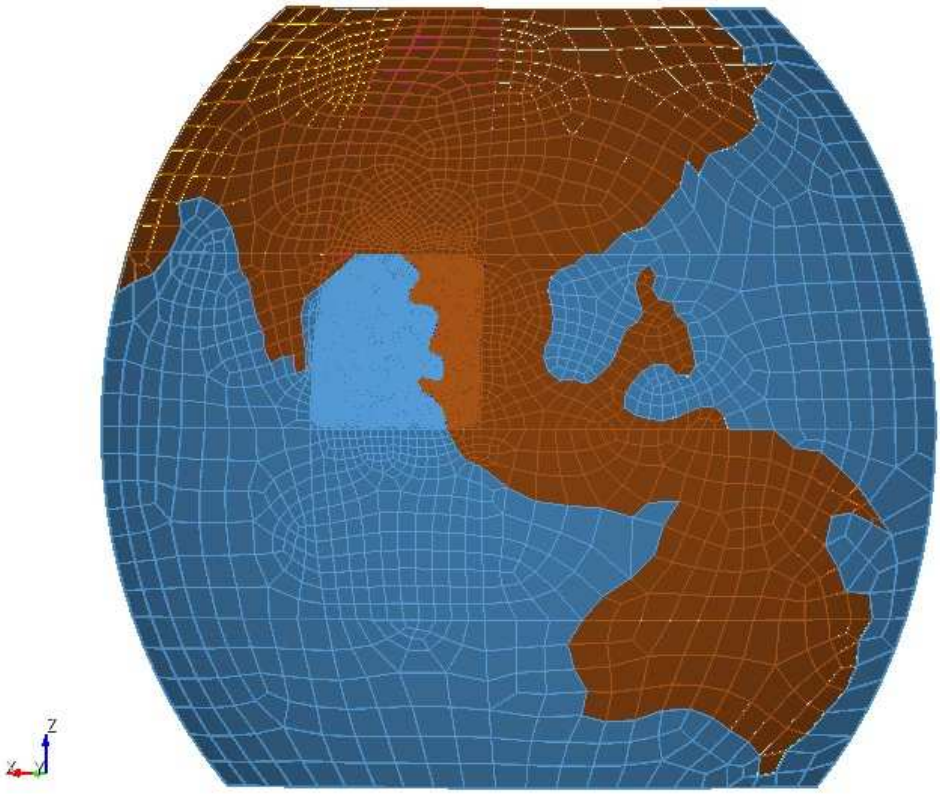

Figure 4: Front view of the unstructured mesh generated by Cubit.

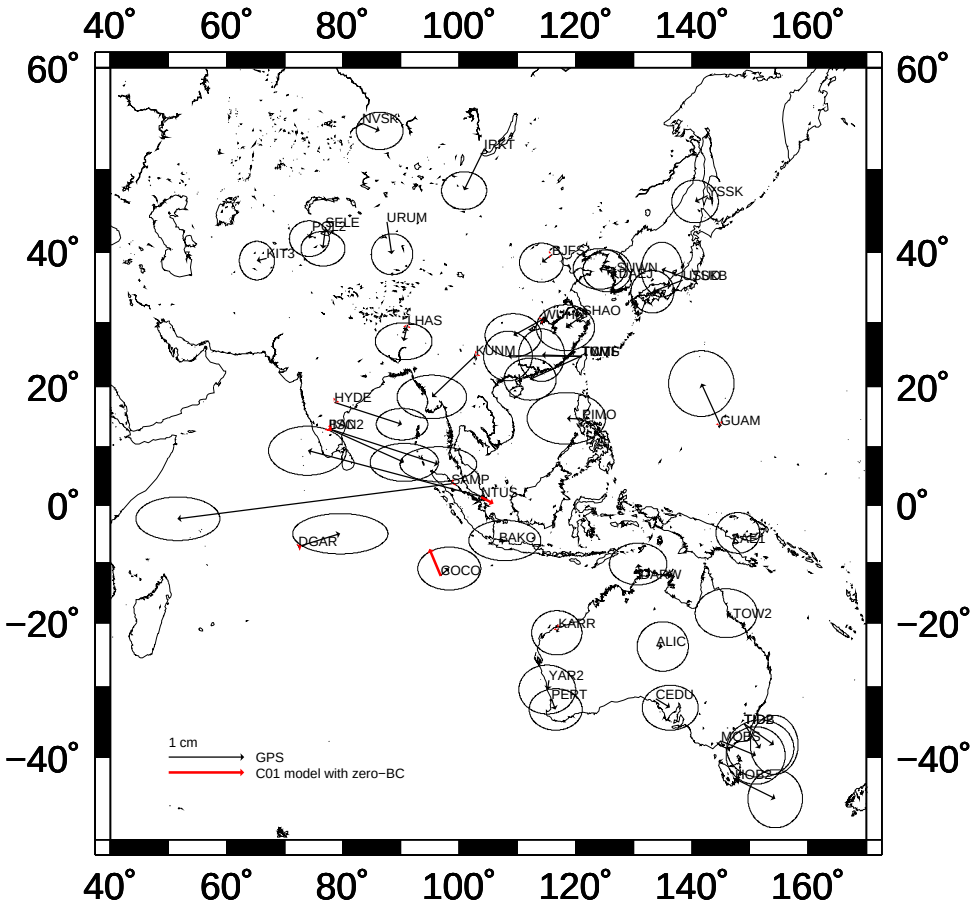

Figure 5: Comparison between GPS measurements from Boschi et al. (2006) and the horizontal displacements resulting from the FE simulations on the C01 model with zero displacement along the boundaries. Error ellipses correspond to 90% confidence.

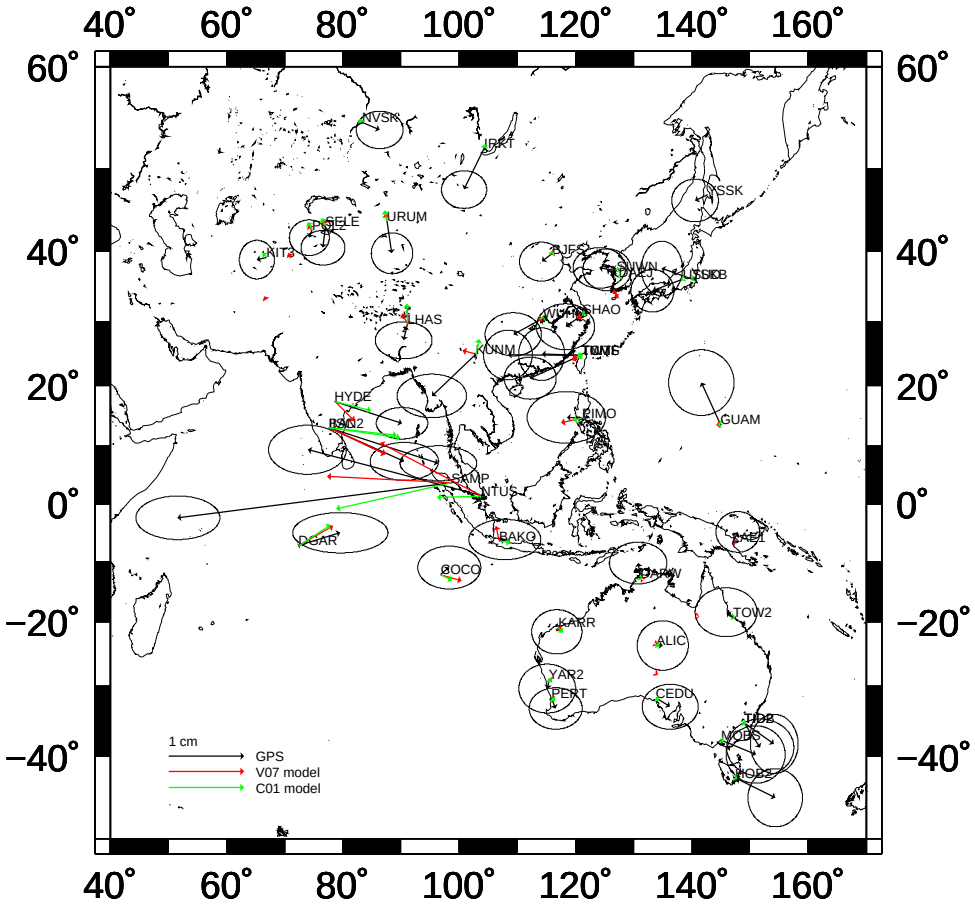

Figure 6: Comparison between GPS measurements from Boschi et al. (2006) and the horizontal displacements resulting from the FE simulations on the V07 and C01 models. Error ellipses correspond to 90% confidence.

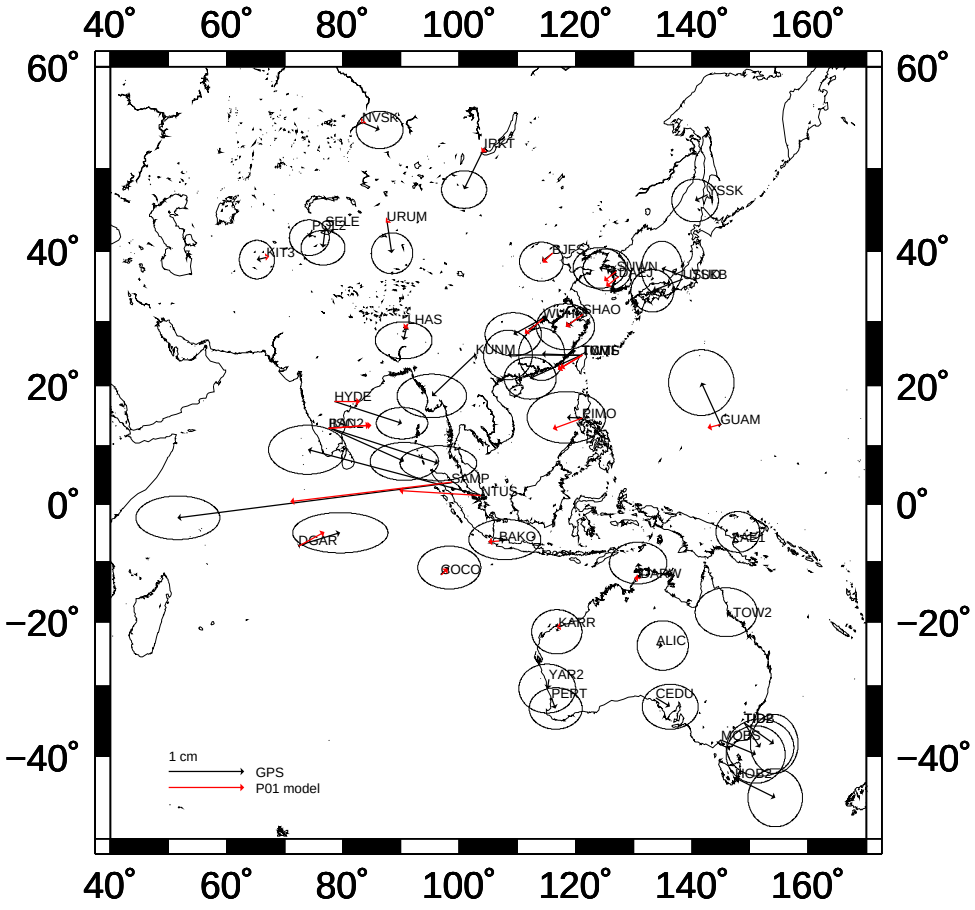

Figure 7: Comparison between GPS measurements from Boschi et al. (2006) and the horizontal displacements resulting from the FE simulation on the flat P01 domain. Error ellipses correspond to 90% confidence.

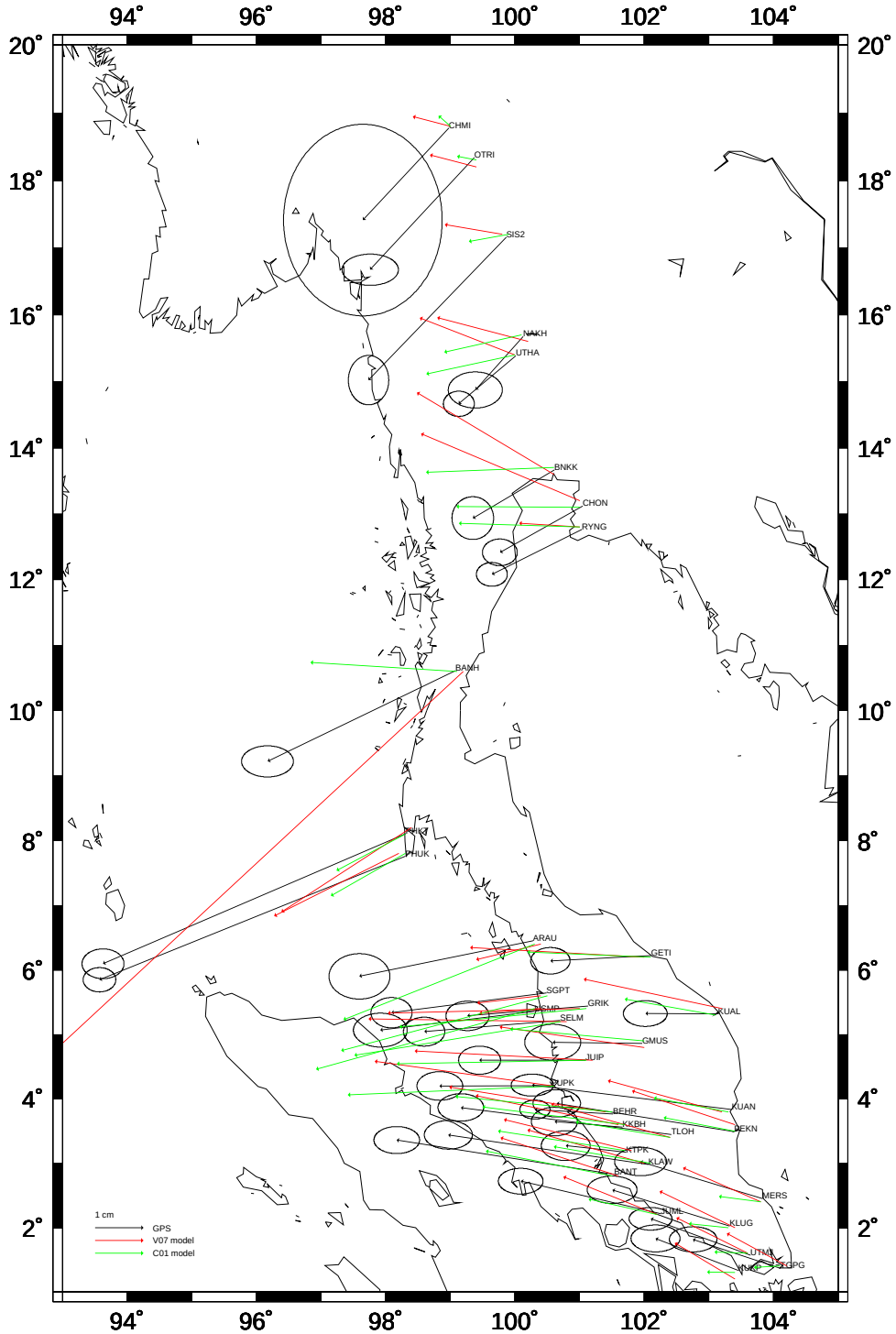

Figure 8: Comparison between GPS measurements from Vigny et al. (2005) and the horizontal displacements resulting from the FE simulations on the V07 and C01 models. Error ellipses correspond to 60% confidence.

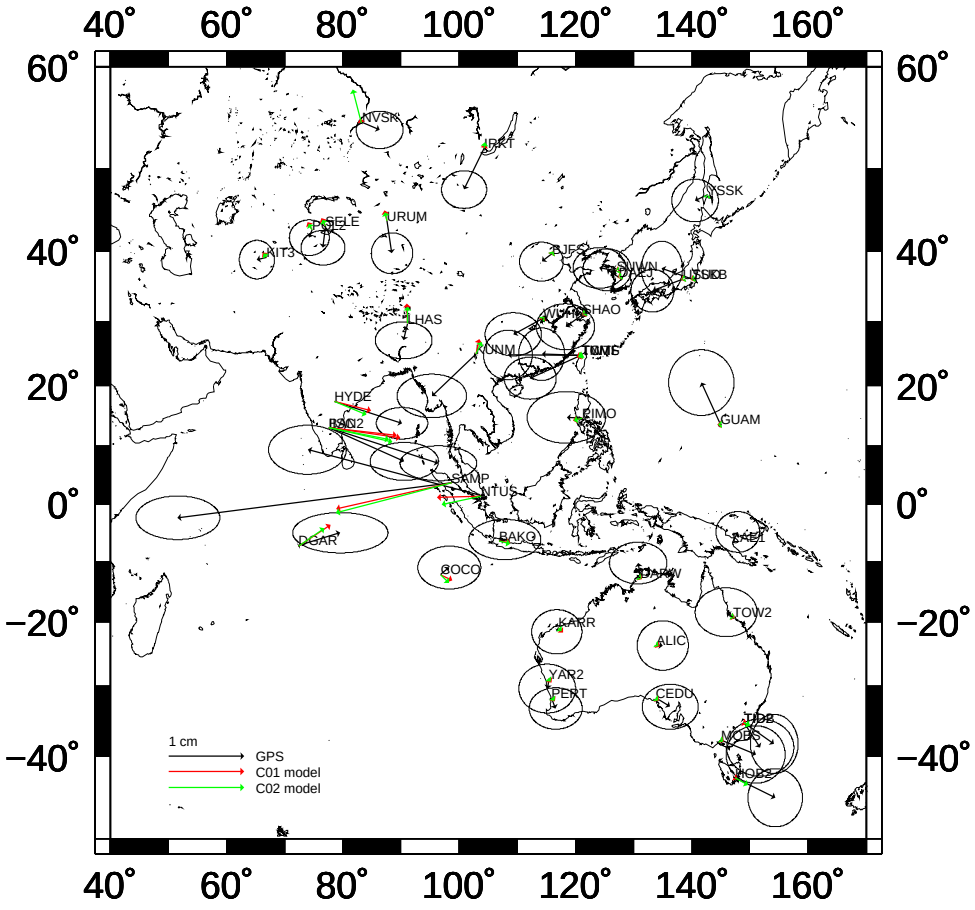

Figure 9: Comparison between GPS measurements from Boschi et al. (2006) and the horizontal displacements resulting from the FE simulations on the C01 and C02 models. Error ellipses correspond to 90% confidence.

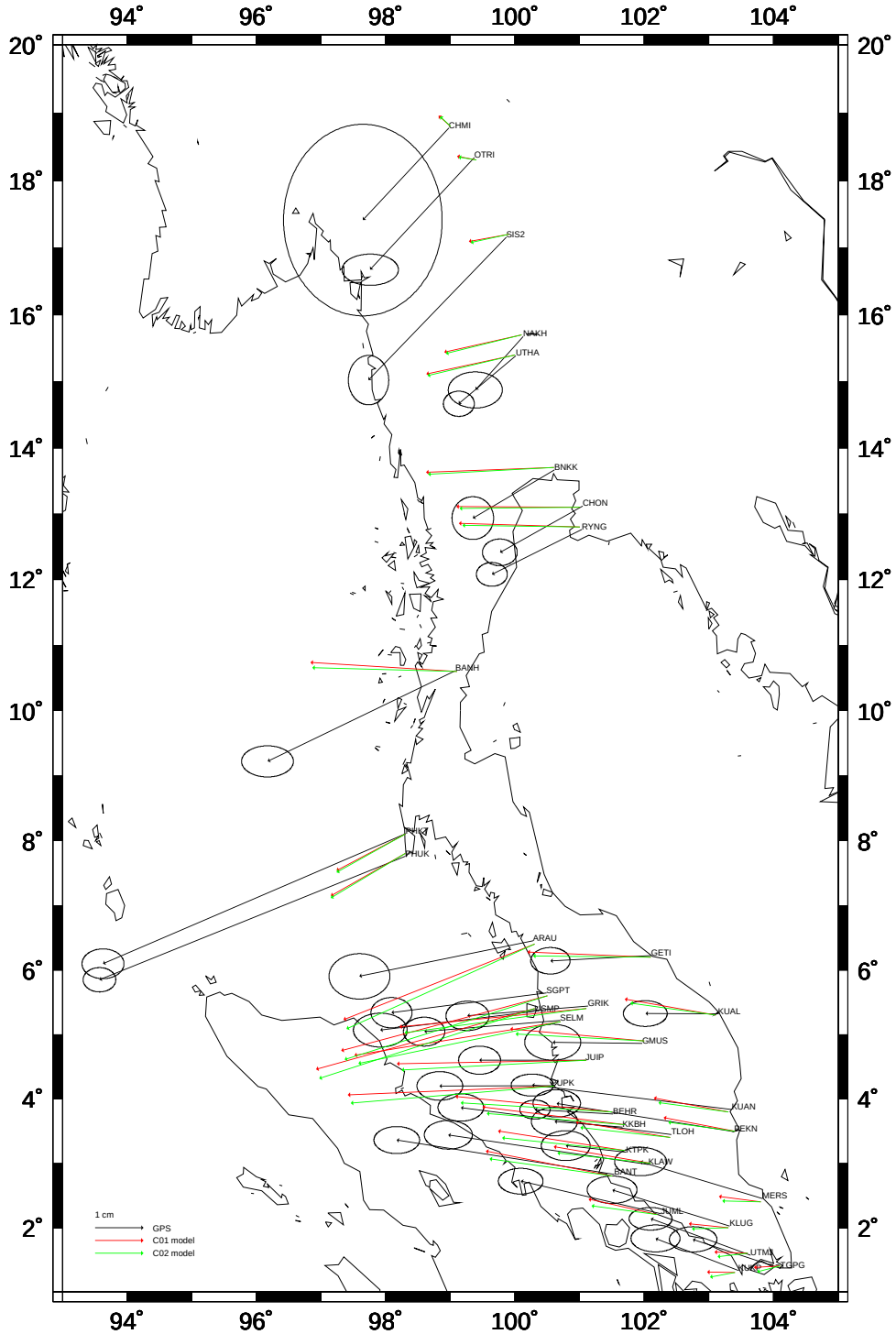

Figure 10: Comparison between GPS measurements from Vigny et al. (2005) and the horizontal displacements resulting from the FE simulations on the C01 and C02 models. Error ellipses correspond to 60% confidence.

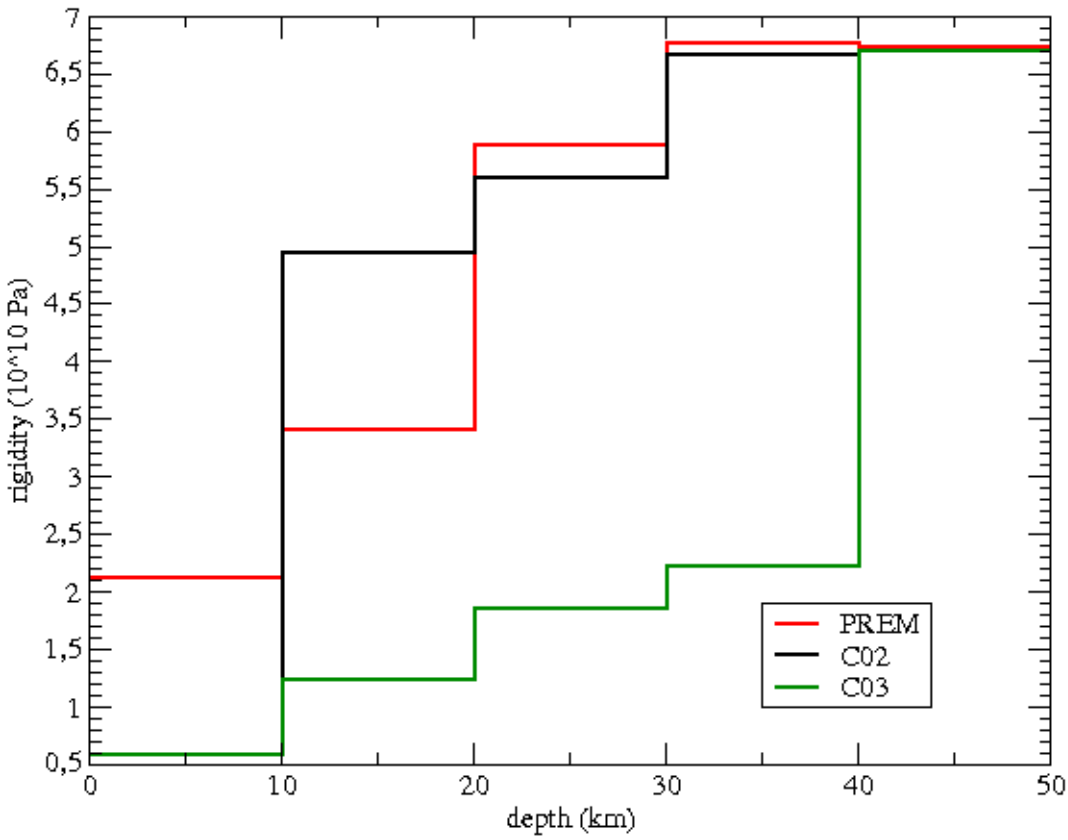

Figure 11: Plot of the (average) rigidity variations with depth in the range 0 0 km in the source region as fixed in the C02 (as well as C01) and C03 models, compared to the PREM values.

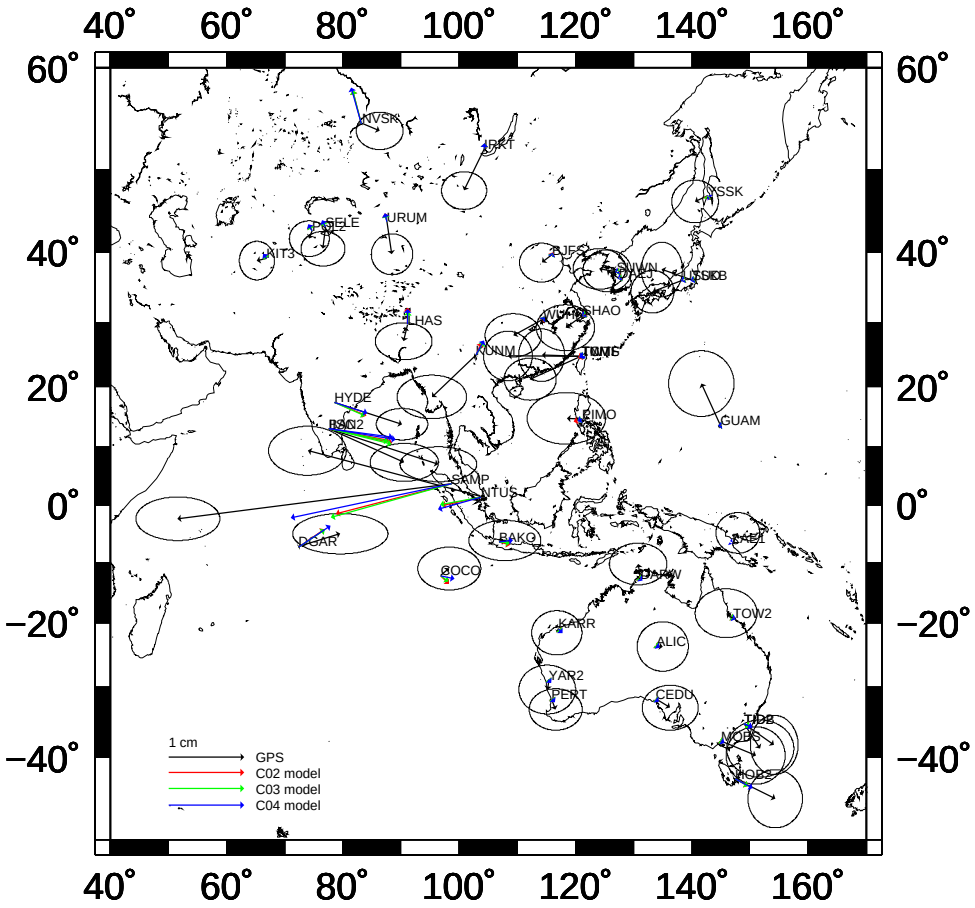

Figure 12: Comparison between GPS measurements from Boschi et al. (2006) and the horizontal displacements resulting from the FE simulations on the C02, C03 and C04 models. Error ellipses correspond to 90% confidence.

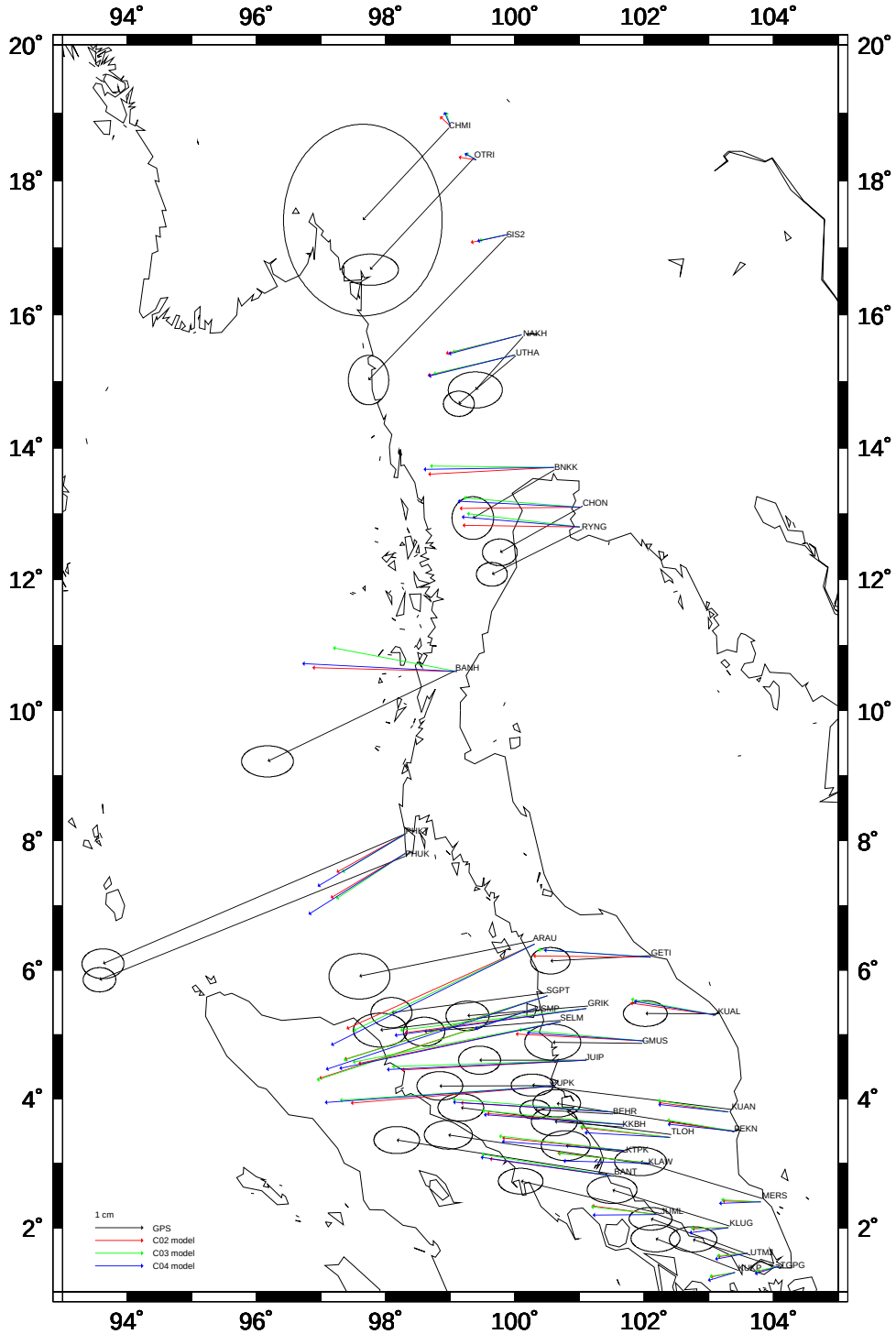

Figure 13: Comparison between GPS measurements from Vigny et al. (2005) and the horizontal displacements resulting from the FE simulations on the C02, C03 and C04 models. Error ellipses correspond to 60% confidence.

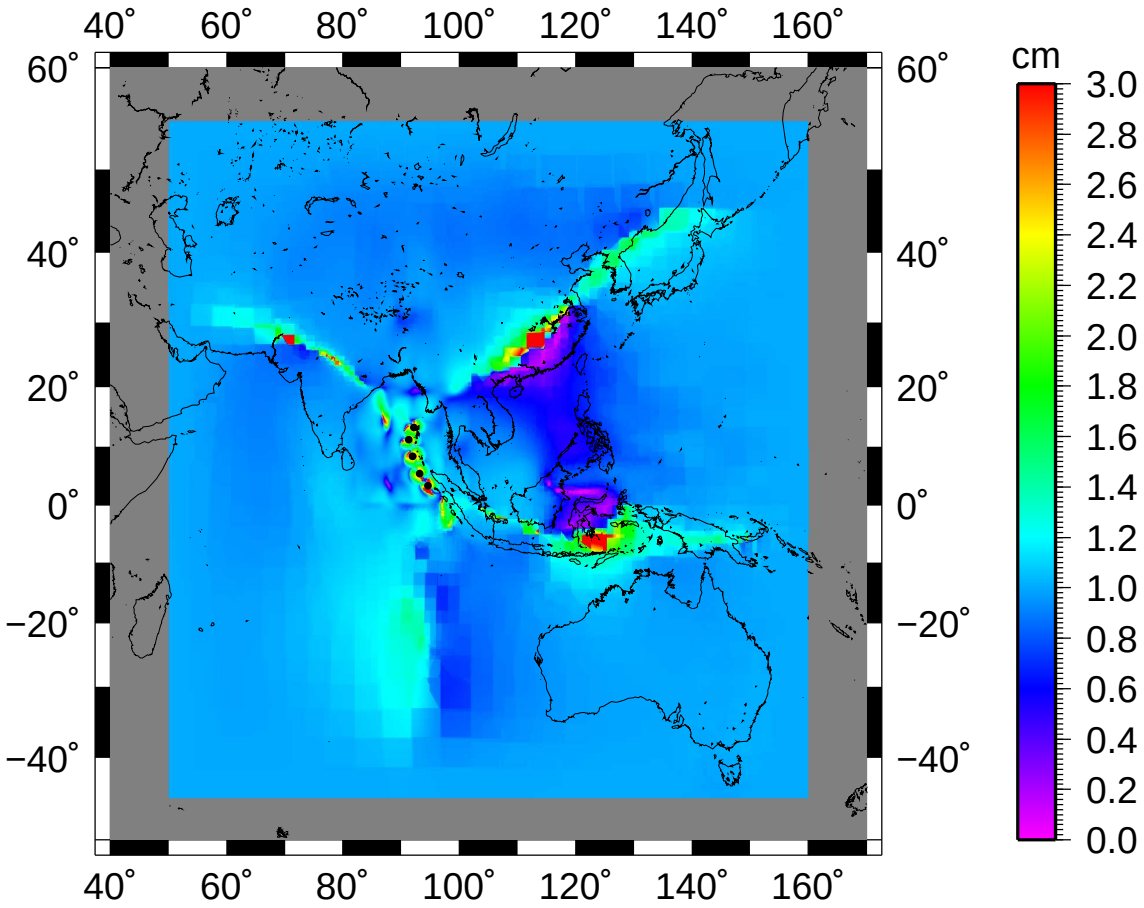

Figure 14: Ratio between the deformation magnitude calculated with the C03 and C02 models.

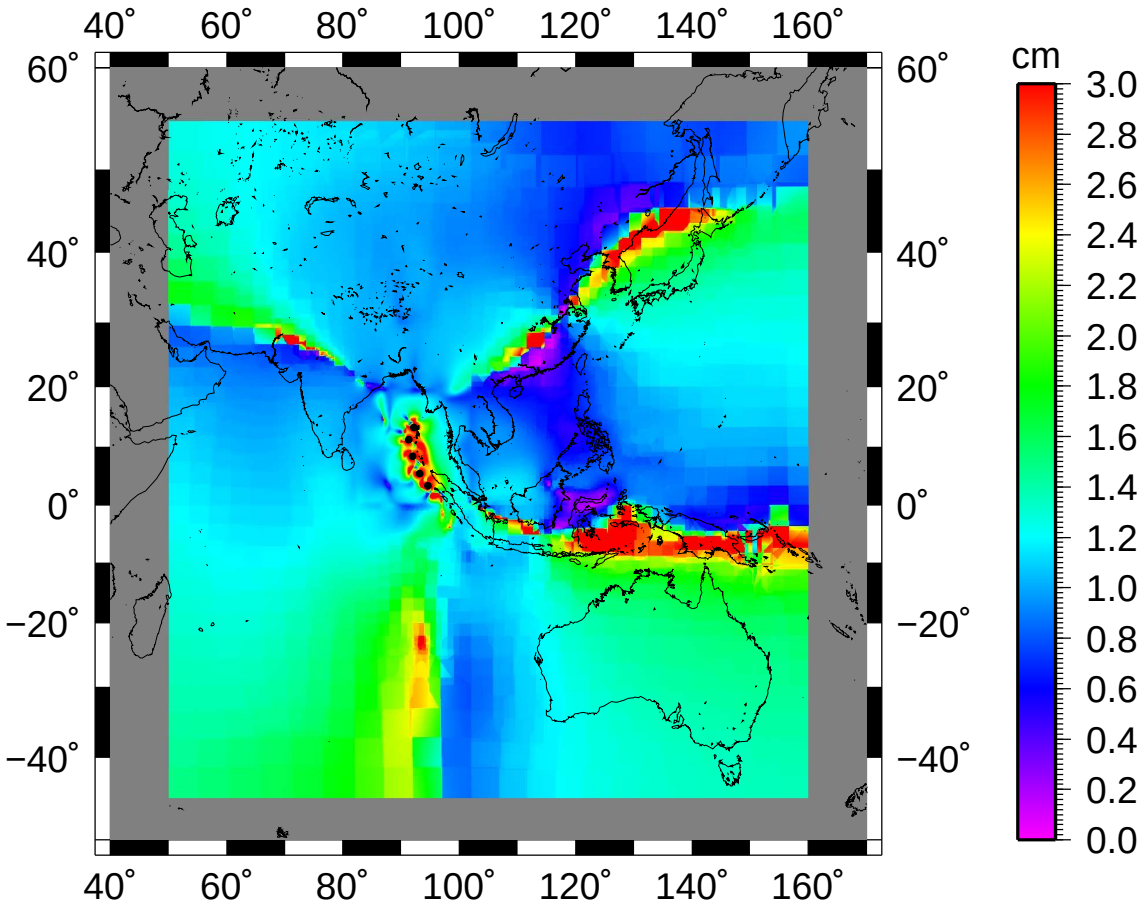

Figure 15: Ratio between the deformation magnitude calculated with the C04 and C02 models.

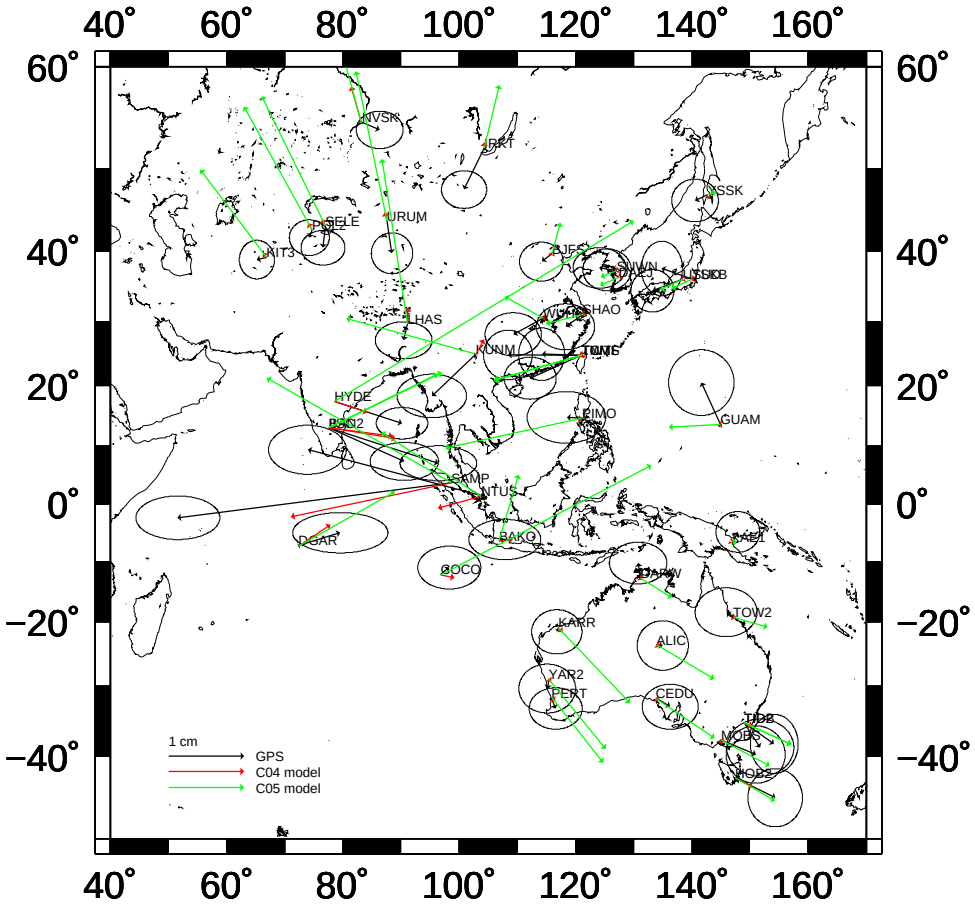

Figure 16: Comparison between GPS measurements from Boschi et al. (2006) and the horizontal displacements resulting from the FE simulations on the C04 and C05 models. Error ellipses correspond to 90% confidence.

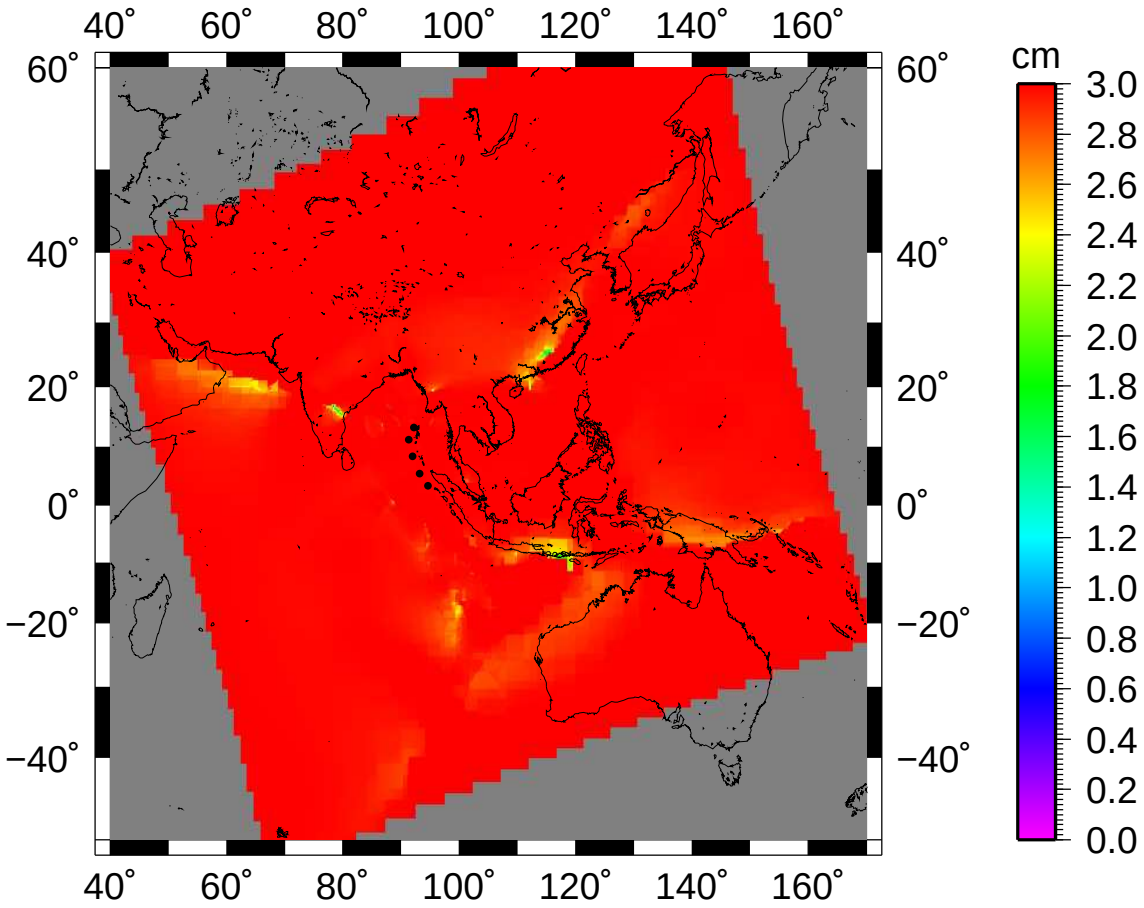

Figure 17: Ratio between the deformation magnitude calculated with C07 and C06 models.

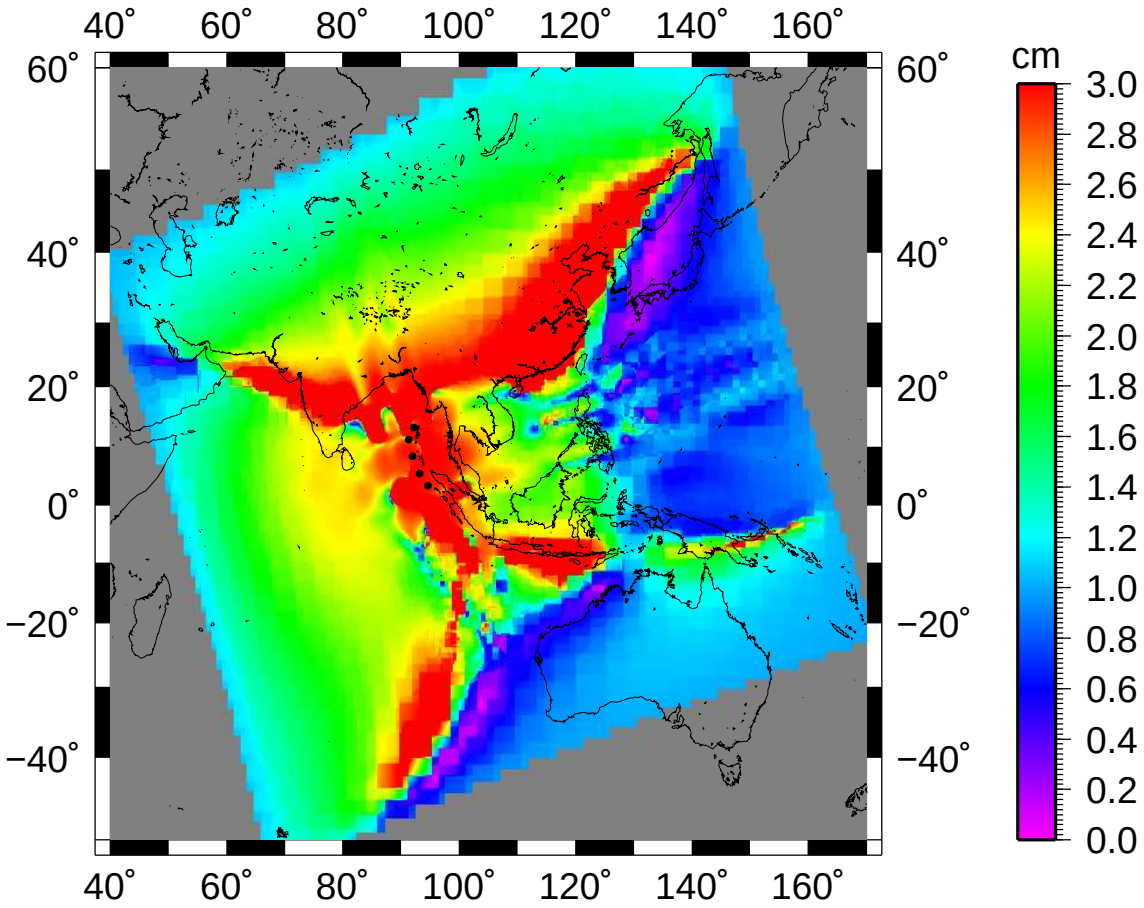

Figure 18: Ratio between the deformation magnitude calculated with C08 and C06 models.